# Chapter 5
# Electron impact ionization of $N_2$ : Energy dependence of e-DDCS, SDCS and TCS

## 5.1 Introduction

When an electron collides with a target molecule, different processes like elastic scattering, excitation, dissociative electron attachment, e-2e, ionization can occur. The energy of the projectile electron with which it collides with the target molecule is the key factor in understanding which process will have higher probability over others. When the energy of the electrons is sufficiently large, then ionization is the most dominant channel. In this mechanism a large amount of energy is transferred from the primary electron to the target, such that an electron is ejected from the target molecule. The electron impact ionization of different target atoms or molecules is not only important for understanding the collision dynamics but is also useful for other fields of research such as, mass spectrometry, plasma physics, astrophysics, stellar atmospheres etc. In this chapter we will discuss about the single ionization of $N_2$ molecules induced by keV energy electrons. Majority of the theoretical and experimental studies for e-impact on $N_2$ have been concentrated with excitation and total ionization cross section [111, 112, 113, 114, 115, 116, 117, 118, 119, 120, 121, 122, 123, 124] with negligible data existing on the DDCS measurements. In the keV energy regime, very few data exists on the detailed measurements of the DDCS of electron emission from $N_2$ [125, 126, 127]. Besides providing information about the contribution of the valence shell electrons in the ionization process, the DDCS measurements also shed light on ionization from inner shells of the target molecule.

## 5.2 Experimental Conditions

A commercially available electron gun(KIMBERLY) capable of generating electrons between 1 and 10 keV was used for the present series of experiments. The details about the experimental setup is already mentioned in chapter 2. In brief, electrons having energies between 3 and 8 keV collided with $N_2$ molecule in the scattering chamber. The projectile velocity varied from 14.85 a.u. to 24.25 a.u. For each beam energy, initially the beam was optimized to achieve maximum beam transmission and then the DDCS measurements were performed both in presence and absence of the target gas. The emitted electrons having energies from 1 eV to 500 eV were collected for several forward and backward angles between $30^0$ and $145^0$. The statistical error

varied from about 2% for the lowest energy electrons to $\sim$ 11% for the high energy electrons in the extreme backward angles. Further details may be obtained from our recent publication [128].

## 5.3 DDCS : Energy Distribution

The measured absolute electron DDCS as a function of emission energy for the five different collision systems have been shown in Figure 5.1, Figure 5.2, Figure 5.3, Figure 5.4 and Figure 5.5. The data have been displayed for different emission angles. Each spectra is seen to fall by several orders of magnitude in the measured emission energy range between 1 and 500 eV, with the cross section being maximum for the lowest energy electrons. The low energy electrons are emitted due to the soft collision mechanism where little momentum transfer takes place yielding maximum cross section in this region. The spectrum then falls rapidly with the increase in the electron emission energies. The sharp peak observed at $\sim$ 350 eV is due to the presence of an inner shell vacancy giving rise to the K-LL Auger electrons. The measured DDCS have been compared with the theoretical CB1 and CTMC model calculations. In case of CB1 model, the partial-wave expansion formalism was used where the incident electron is described by a plane wave. The projectile electron after getting scattered is also described by a plane wave whereas the emitted electron is modelled by a Coulomb wave [62] with an effective target charge $Z_T^* = \sqrt{-2n^2\epsilon}$, here $n$ is the principal quantum number of each atomic orbital component used in the molecular target description and the active electron orbital energy $\epsilon$ is related to the ionization energies $B$ of each occupied molecular orbital by $\epsilon = -B$. For the DDCS calculations, the $N_2$ target molecule was described using two different descriptions of the molecular wave functions i.e., the RHF/6-311G and CCSD/cc-pVTZ levels of the theory. The RHF/6-311G is a simple restricted Hartree-Fock description of the target with the medium accuracy Pople basis set 6-311G. The CCSD/cc-pVTZ description is a coupled cluster calculation using both single and double substitutions from the Hatree-Fock determinant along with a much larger Dunning's correlation-consistent polarized basis set with triple-zeta. The first ionization energy corrected for zero-point vibrational energy (ZPE) was 16.900 eV with RHF/6-311G and 16.527 eV with CCSD/cc-pVTZ using Koopman's theorem. The ionization energy was further constrained to match the experimental value of 15.581 $\pm$ 0.008 for $N_2$ in the gas phase [129]. This exercise was performed to assess the possible impact of different descriptions of $N_2$ molecular wave functions on the DDCS.

In case of the calculations using the CTMC model, the $N_2$ molecule was considered as two N atoms. Here the classical equations of motions are solved numerically [130, 67, 131, 132]. The many-electron target atom was replaced by a one-electron atom and the projectile was considered as one particle [133]. The target atom was described by a central model potential

based on the Hartree-Fock method [68]. The potential can be written as:

$$V(r) = q\frac{Z - (N-1)\left(1 - \Omega^{-1}(r)\right)}{r} = q\frac{Z(r)}{r}, \tag{5.1}$$

where $Z$ is the nuclear charge, $N$ is the total number of electrons in the atom or ion, $r$ is the distance between the nucleus and the test charge $q$, and

$$\Omega(r) = \frac{\eta}{\xi}\left(e^{r\xi} - 1\right) + 1. \tag{5.2}$$

The potential parameters $\xi$ and $\eta$ were obtained in such a way that they minimize the energy for a given atom [134]. For N atom, $\xi$ and $\eta$ were 1.179 a.u. and 2.27 a.u respectively. Such a potential has a correct asymptotic form for both the small and large values of $r$.

Newton's classical non-relativistic equations of motion for a three-body system were solved numerically for a statistically large number of trajectories for given initial conditions. In the present case, an ensemble of 5 x $10^7$ trajectories were used. The equations of motion were solved using the standard Runge-Kutta method [135]. The initial conditions of the individual collisions are chosen at sufficiently large internuclear separations from the collision center, where the interactions among the particles are negligible [136]. A microcanonical ensemble characterizes the initial state of the target. The initial conditions were taken from this ensemble such that initial binding energies of the N(2p) level ($E_b$ = -0.5343 a.u.) and N(2s) level ($E_b$ = -1.371 a.u.) were constrained. For ionization channel the energy and the scattering angles of the particles were recorded. These parameters were calculated at large separation of the projectile and the target nucleus.

The double differential cross-sections were computed using the following formula:

$$\frac{d^2\sigma}{dEd\Omega} = \frac{2\pi b_{max}}{T_N \Delta E \Delta\Omega}\sum_j b_j^{(i)}. \tag{5.3}$$

Further the total cross sections are generated as :

$$\sigma = \frac{2\pi b_{max}}{T_N}\sum_j b_j^{(i)}, \tag{5.4}$$

In Equation 5.3 and Equation 5.4, $T_N$ is the total number of trajectories calculated for impact parameters less than $b_{max}$, and $b_j^{(i)}$ is the actual impact parameter for the trajectory corresponding to the ionization process under consideration in the energy interval $\Delta E$ and the emission angle interval $\Delta\Omega$ of the electron.

In Figure 5.1, for 3 keV $e^-$ impact on $N_2$, we have displayed the theoretical DDCS predicted by the CB1 model using both the molecular wave functions, i.e, the RHF/6-311G (black solid line) and CCSD/cc-pVTZ (magenta dash-dotted line) along with experimentally measured DDCS. It is seen that in the log-log scale, the two models almost merge together. This indicates that at such high projectile energy (few keV) the use of different descriptions of the

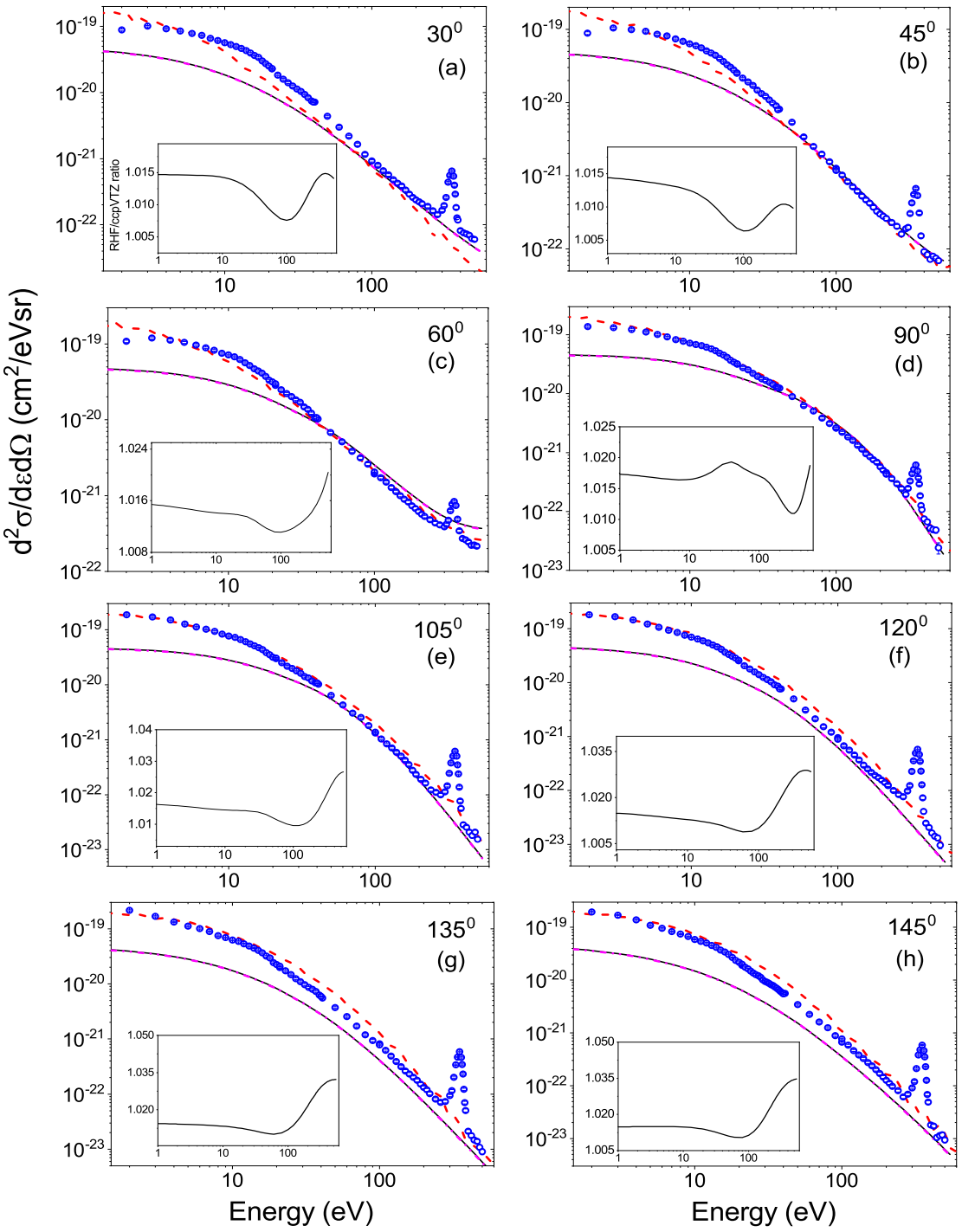


Figure 5.1: The absolute electron DDCS for the collision system 3 keV $e^-$ + $N_2$, at different emission angles. The black solid line and the magenta dash-dotted line represent the CB1 calculations using the RHF/6-311G and CCSD/cc-pVTZ descriptions of the target wave functions respectively. The red dashed line corresponds to the DDCS predictions of the CTMC model. Inset : DDCS ratio using RHF and ccpVTZ descriptions of target wave functions.

molecular wave functions have negligible impact on the DDCS calculations. However, in order to understand the difference in DDCS using the two different wave functions quantitatively, the ratio between the CB1 predictions is shown in the inset of each panel in Figure 5.1. The ratio

is seen to vary between 1.01 to 1.04. Overall the CB1 calculations show a qualitative agreement with the experimental data points, although quantitatively there are deviations. In case of the forward angles, the calculations underestimate the data upto about 60 eV, beyond which it shows good agreement with the data. For the intermediate angles, around $90^0$, the theory shows good agreement with the measured DDCS above 50 eV. However, in case of backward angles, the model underestimates the data over the entire spectra, with maximum discrepancy occurring for the low emission energies.

The red dashed line in each panel in Figure 5.1 corresponds to the CTMC calculations for twice of atomic nitrogen. Overall a good agreement is observed with this model over the entire energy regime. A closer look at Figure 5.1 shows that in the forward angle ($30^0$), the model underestimates the data points, although this difference vanishes with the increase in the emission angles.

Similarly, for 4 keV $e^-$, (Figure 5.2), the CB1 model shows qualitative agreement with deviations existing in the low energy region for forward angles and large deviations in case of backward angles. CTMC predictions on the other hand, matches very well with the data except below 10 eV, where it overestimates the experimental values. For the backward angles ($135^0$ and $145^0$), the CTMC calculations are slightly higher than the measured DDCS over the entire energy range under investigation. It is further noticed that the shape of the DDCS spectrum changes around $90^0$ compared to that seen in the forward and backward angles. This change may be explained by the dominance of the binary encounter process between the projectile and target electrons.

In case of 5 keV $e^-$ impact measurements (Figure 5.3), although CB1 predicts lower cross section compared to experimental values, but the difference is less than that seen in Figure 5.1 and Figure 5.2. From 3 and 4 keV impact energies, it is seen that there is almost no difference in the DDCS calculations obtained from the two different descriptions of the target wave functions. Hence from here onward, the CB1 calculations using the RHF/6-311G description have been plotted along with the experimental data. The CTMC calculations again matches well with the experimental DDCS except below 20 eV for forward angles where it overestimates the data. It is further observed that below 15 eV, there is a minor fall in the experimental data points at the backward angles. This fall could be due to the presence of some stray electric or magnetic field which might have caused hindrance to the collection of these low energy electrons.

Similarly, for 6 keV (Figure 5.4) and 8 keV impact electrons (Figure 5.5), the CB1 calculations (black solid line) underestimate the measured DDCS for $30^0$, whereas with the increase in emission angle, i.e., for $80^0$, $90^0$ and $105^0$, the calculations are seen to have good agreement with the data beyond 50 eV. However, at the backward angles, theory although shows a qualitative agreement, but underestimates the data, as seen in case of the other beam energies. The sharp peak seen at $\sim$ 350 eV corresponds to the Auger electron emission. The theoretical calculations using the CTMC model were not available for 6 and 8 keV beam energies and hence, are not displayed in Figure 5.4 and Figure 5.5.

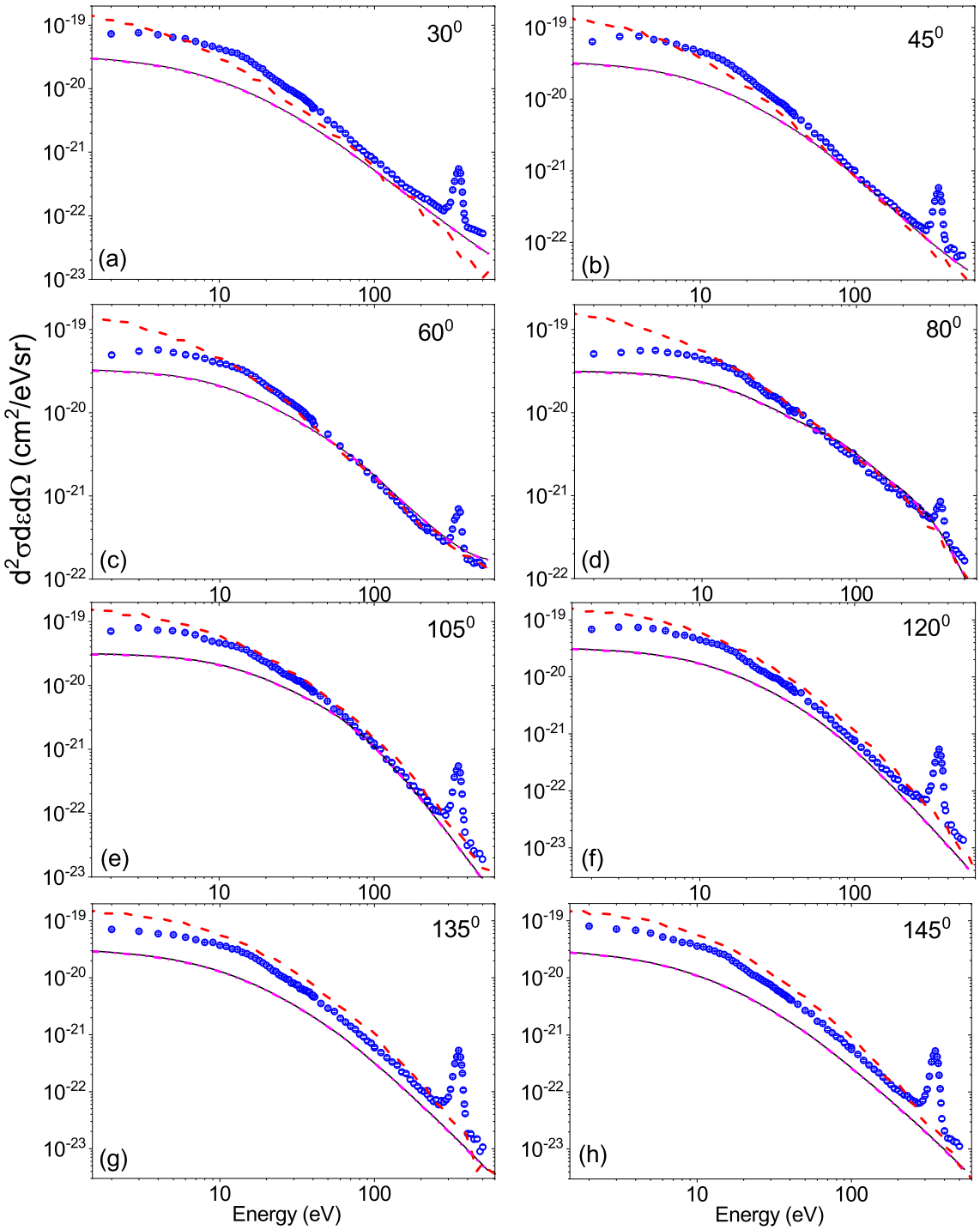


Figure 5.2: Absolute electron DDCS for the collision system 4 keV $e^-$ + $N_2$, at different emission angles; CB1 calculations using the RHF/6-311G (black solid line) and CCSD/cc-pVTZ (magenta dash-dotted line) descriptions of the target wave functions. Red dashed lines represent the DDCS using CTMC model.

Figure 5.6 displays the calculated DDCS using the CB1 model with the RHF/6-311G description of the target wave function for 3 keV electron impact on $N_2$ as a function of the ejected electron energy for various emission angles. It may be noticed that in the lowest energy region, all the curves corresponding to the different emission angles bunch together. This region is

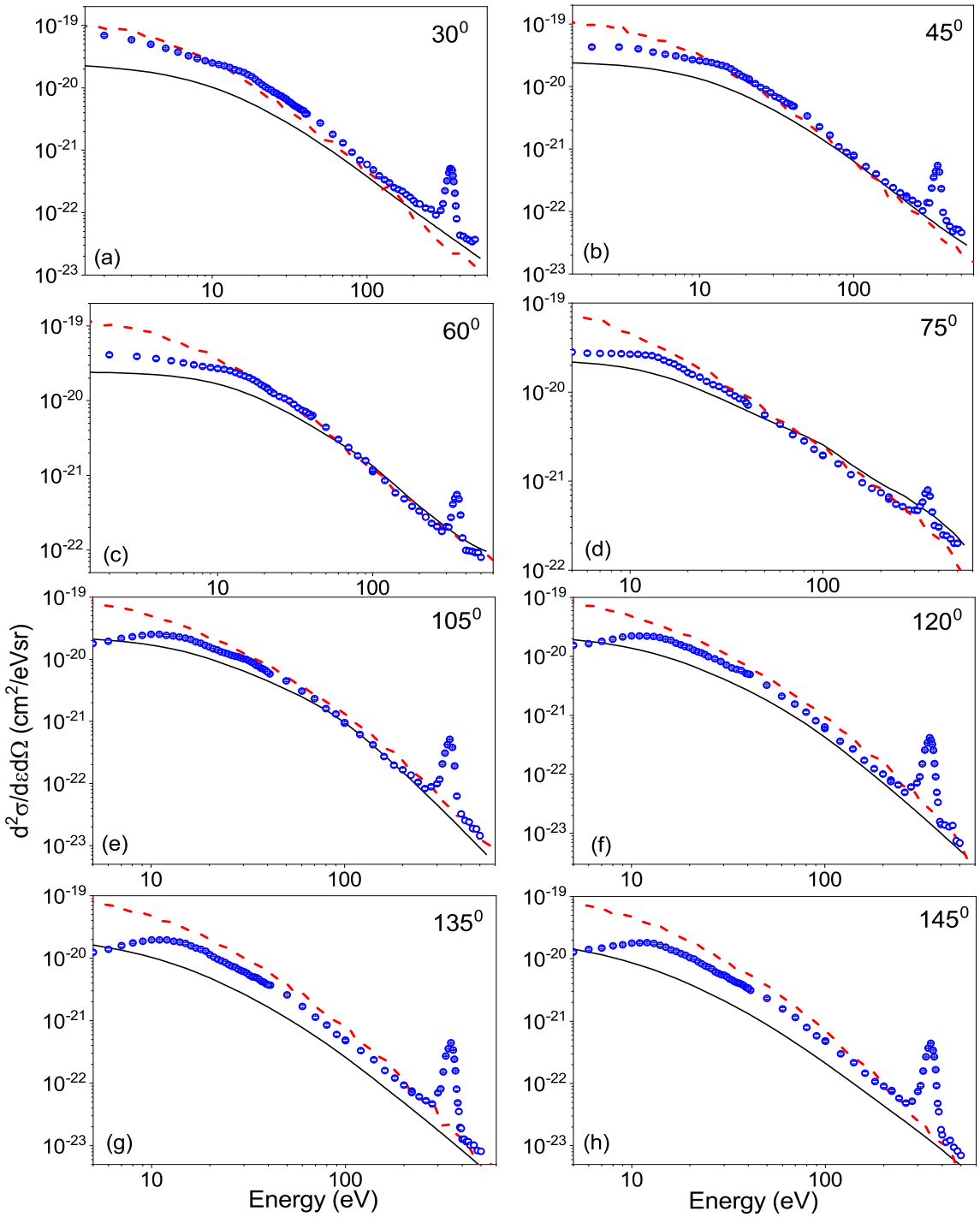


Figure 5.3: Absolute electron DDCS for the collision system 5 keV $e^-$ + $N_2$. Black solid line shows CB1 calculations using the RHF/6-311G description of the target wave function and the red dashed lines are those using the CTMC model.

dominated by the soft collision mechanism for which the DDCS remains almost independent of the emission angles. With the increase in the emission energies, although the cross section starts falling for all the angles, but, for the intermediate angles (i.e., $75^0$, $80^0$ and $90^0$) the fall in the DDCS spectra is not as rapid as that seen for the forward and backward angles. There is a change in shape of the DDCS for the intermediate angles and this difference among the dif-

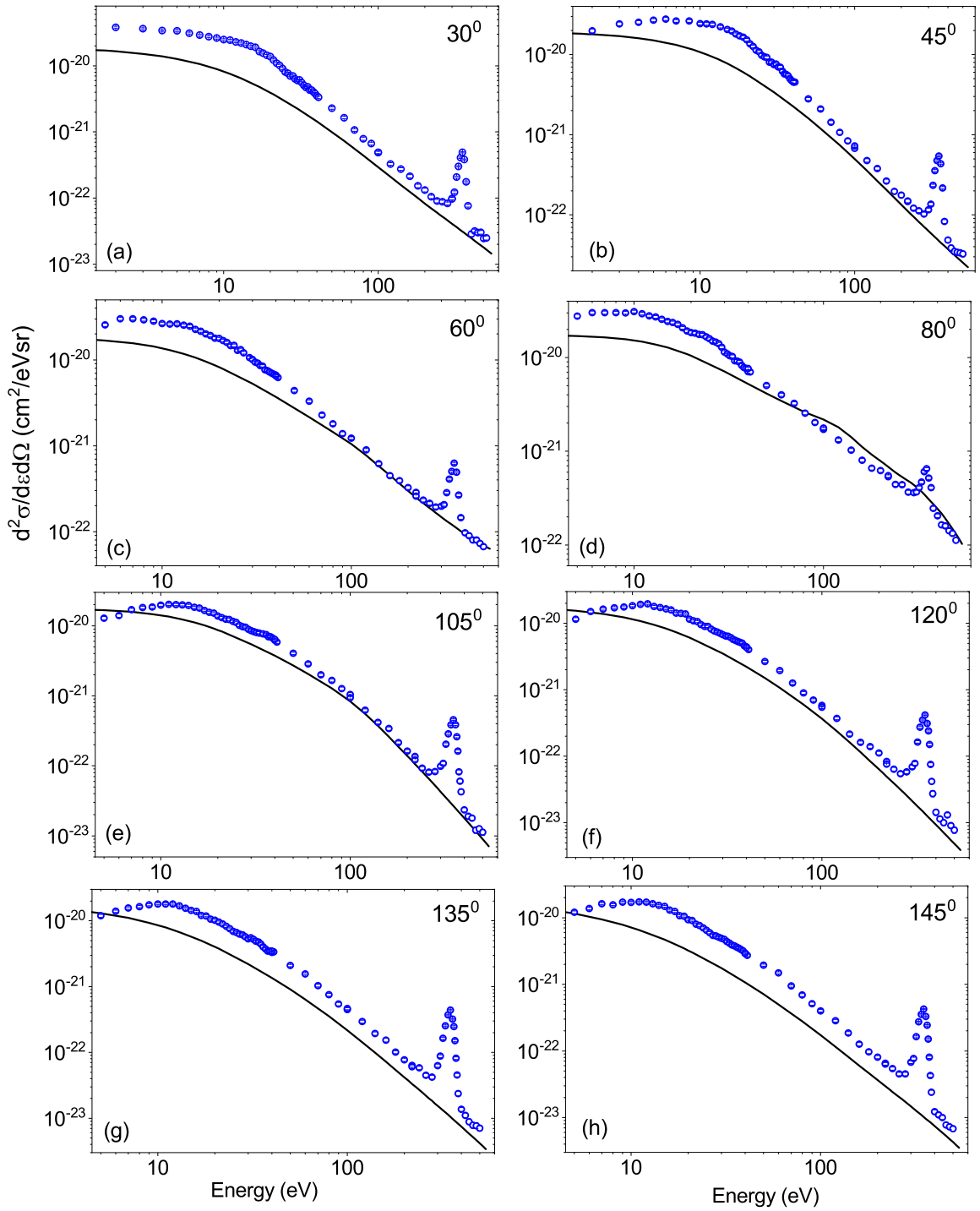


Figure 5.4: Absolute electron DDCS for the collision system 6 keV $e^-$ + $N_2$. CB1 calculations using the RHF/6-311G target wave function are shown by the black solid lines.

ferent lines in Figure 5.6 represent the angular distributions which is discussed in the following section.

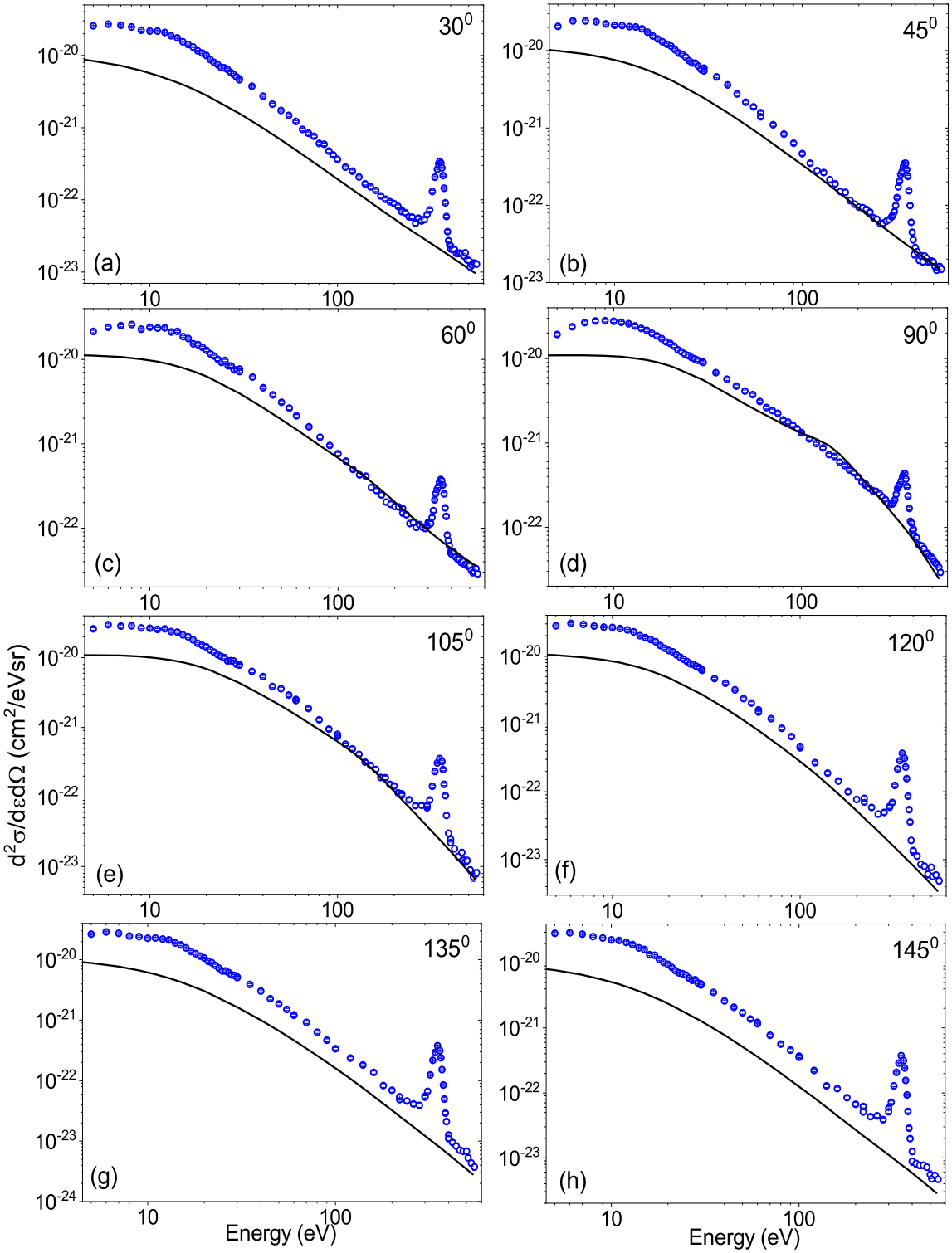


Figure 5.5: Same as Figure 5.4, but for the collision system 8 keV $e^-$ + $N_2$.

## 5.4 DDCS : Angular Distribution

To have a better understanding of the features seen in Figure 5.6, the absolute DDCS of the ejected electrons as a function of different emission angles have been displayed in Figure 5.7,

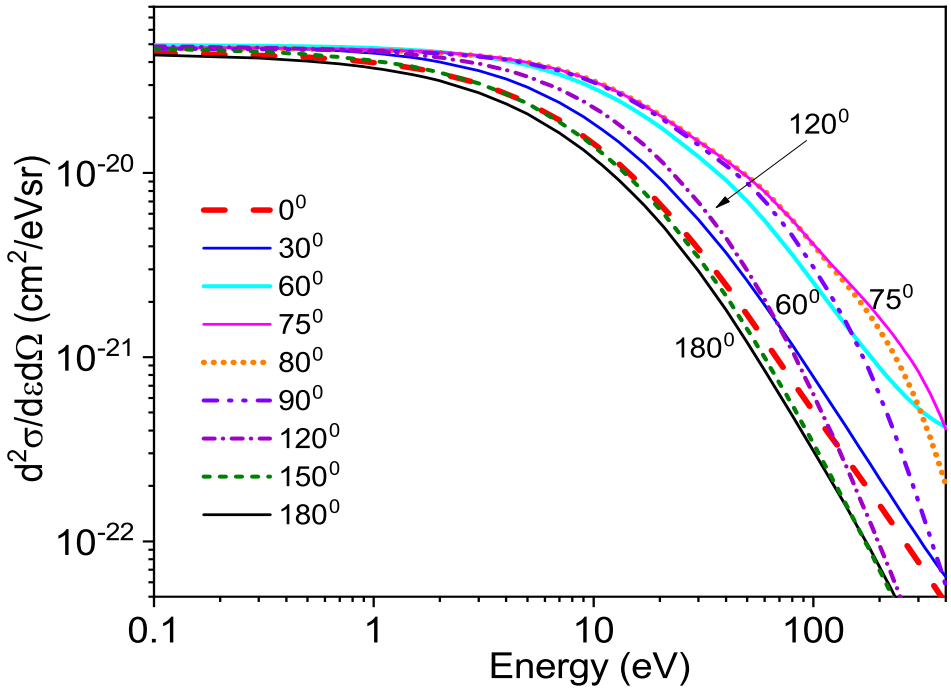


Figure 5.6: Theoretical (CB1) DDCS for different emission angles for 3 keV projectile electron beam

Figure 5.8, Figure 5.9, Figure 5.10 and Figure 5.11 corresponding to the projectile beam energies 3, 4, 5, 6 and 8 keV respectively. It may be mentioned that since the energy distribution spectra fall by 3-4 orders of magnitude, it is difficult to explore the finer details of the difference between the experimental measurements and the theoretical DDCS predictions. The angular distributions at fixed emission energies serve the purpose. The eight plots shown in Figure 5.7 expand over the entire emission energy range showing signature of different features of collision mechanisms at different parts of the spectrum. In Figure 5.7(a), an almost flat distribution is observed for 7 eV, corresponding to the soft collision mechanism which is dominated by large impact parameter events. For higher electron emission energies, a peak like structure starts appearing around $80^0$ which sharpens further with the increase in the emission energies. This peak is due to the binary nature of collision i.e. the direct two-body free-electron scattering between the incident electron and the target electron while the recoil-ion remains passive. In case of electron impact ionization, the position of the binary peak is obtained from the following relation $\theta_b = cos^{-1}(\sqrt{\frac{e}{E_0}})$, where $e$ is the ejected electron energy and $E_0$ is the projectile electron energy. For emission energy of 200 eV, the calculated peak position is $75.04^0$. This is seen to be matching well with the experimental observation in Figure 5.7(g), where the highest yield is observed at $75^0$. Further, in Figure 5.7, the CB1 model using the two different molecular wave functions (black solid and magenta dash-dotted lines) show a qualitative agreement with the measurements. The model calculations underestimate the data quantitatively, except in the peak region, where it matches well with the data points. With the increase in the emission

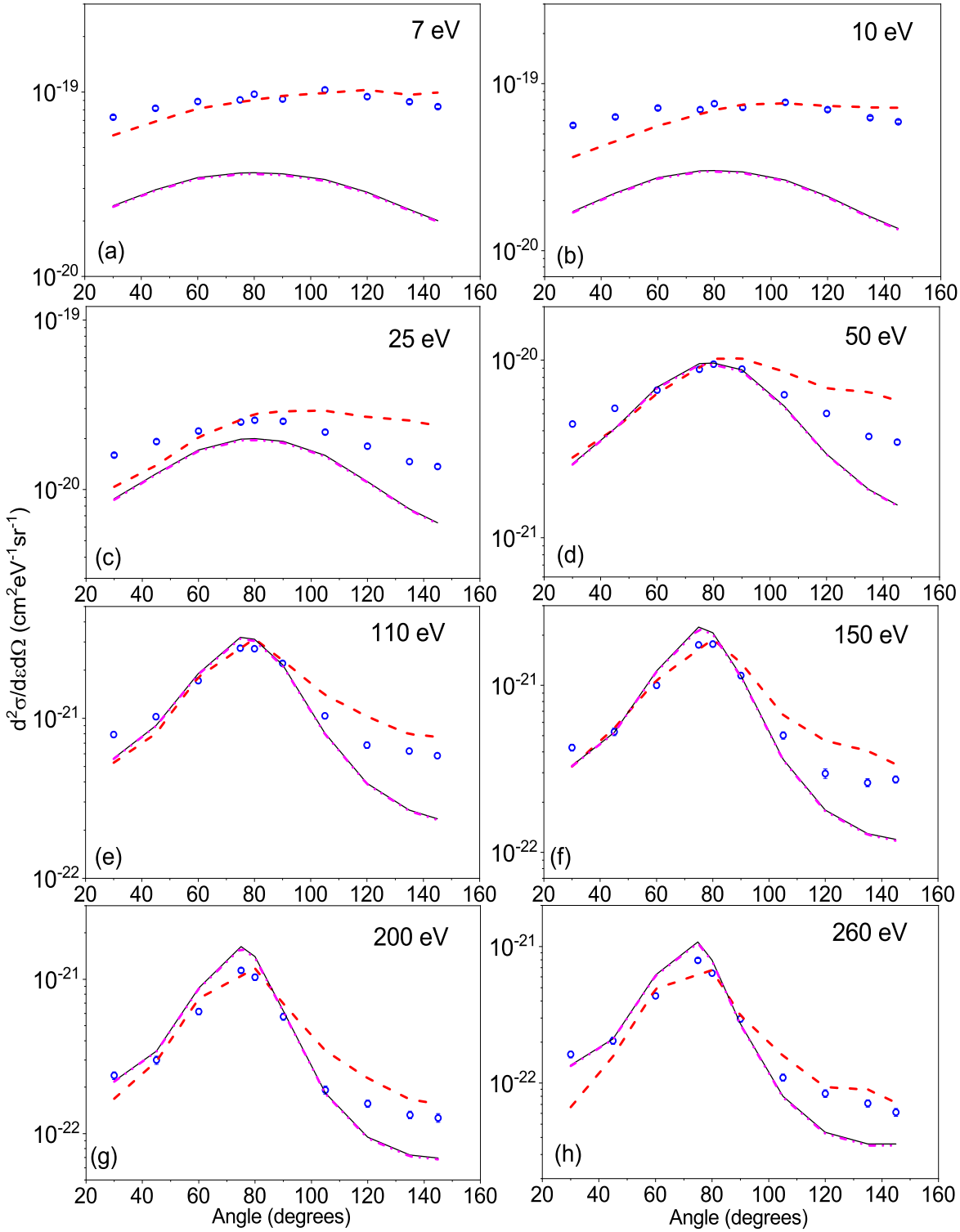


Figure 5.7: Absolute e-DDCS for the collision system 3 keV $e^-$ + $N_2$, at different emission energies. Legends are similar to those described in Figure 5.1.

energies, it is seen that the DDCS values for the forward angles are slightly higher compared to those for the backward angles. Similar features are also observed in Figure 5.8, Figure 5.9, Figure 5.10 and Figure 5.11. In all the cases, the CB1 model underestimates the data for the low emission energies, however, for higher energies it matches well or slightly overestimates

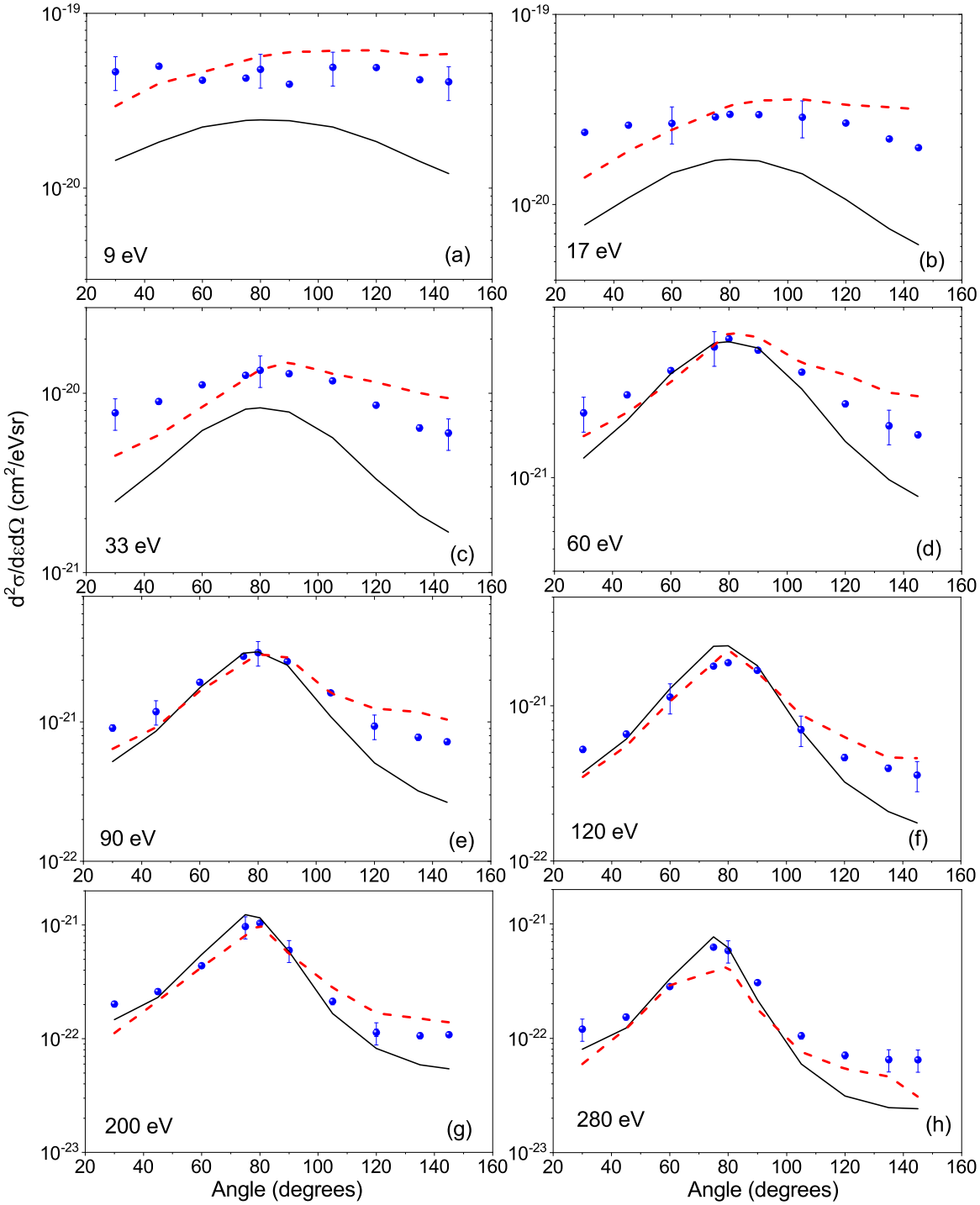


Figure 5.8: e-DDCS for the collision system 4 keV $e^-$ + $N_2$, at different emission energies. Black solid line : CB1 calculations using the RHF/6-311G description of the target wave functions, red dashed line : CTMC model for 2N.

the measured data near the binary peak and underestimates the data for the backward angles. In Figure 5.8, the absolute error bars are shown for some of the data points, whereas in all the other figures the error bars due to statistical fluctuations are shown, which are mostly within symbol size and hence not visible.

In case of Figure 5.7, Figure 5.8 and Figure 5.9, the red dashed lines correspond to the

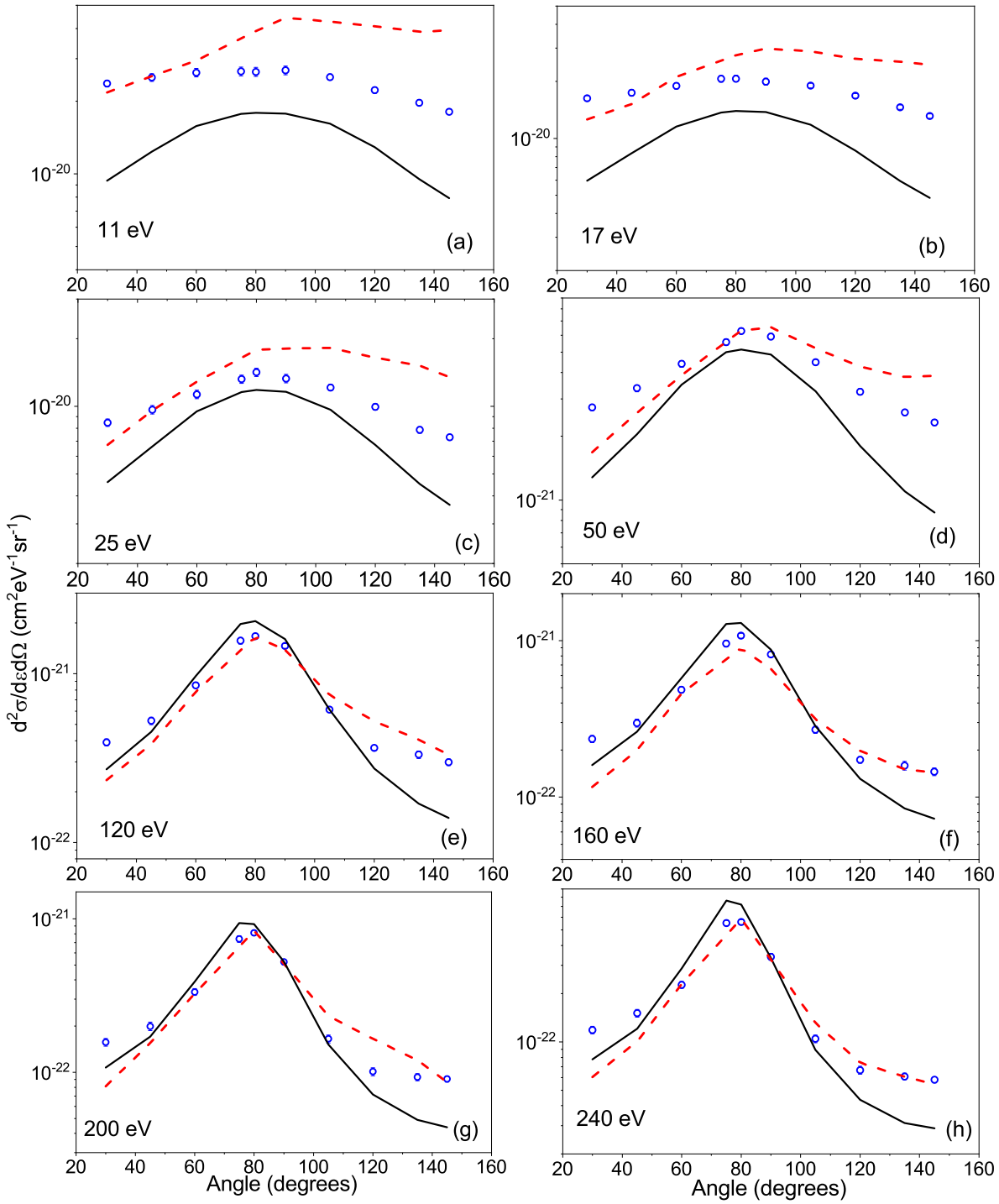


Figure 5.9: Same as Figure 5.8, except for collision system : 5 keV $e^-$ + $N_2$.

calculations using the CTMC model. In Figure 5.7(a), at 7 eV, the CTMC calculation show an excellent agreement with the data. However, with increase in emission energies, it is observed that the CTMC model predicts a higher cross section for the backward angles compared to that for the forward angles. It is seen that the forward-backward angular asymmetry is not reproduced properly by the CTMC model unlike the cases for the experimental measurements and the CB1 model. This behaviour is seen for all the three projectile energies, where the CTMC

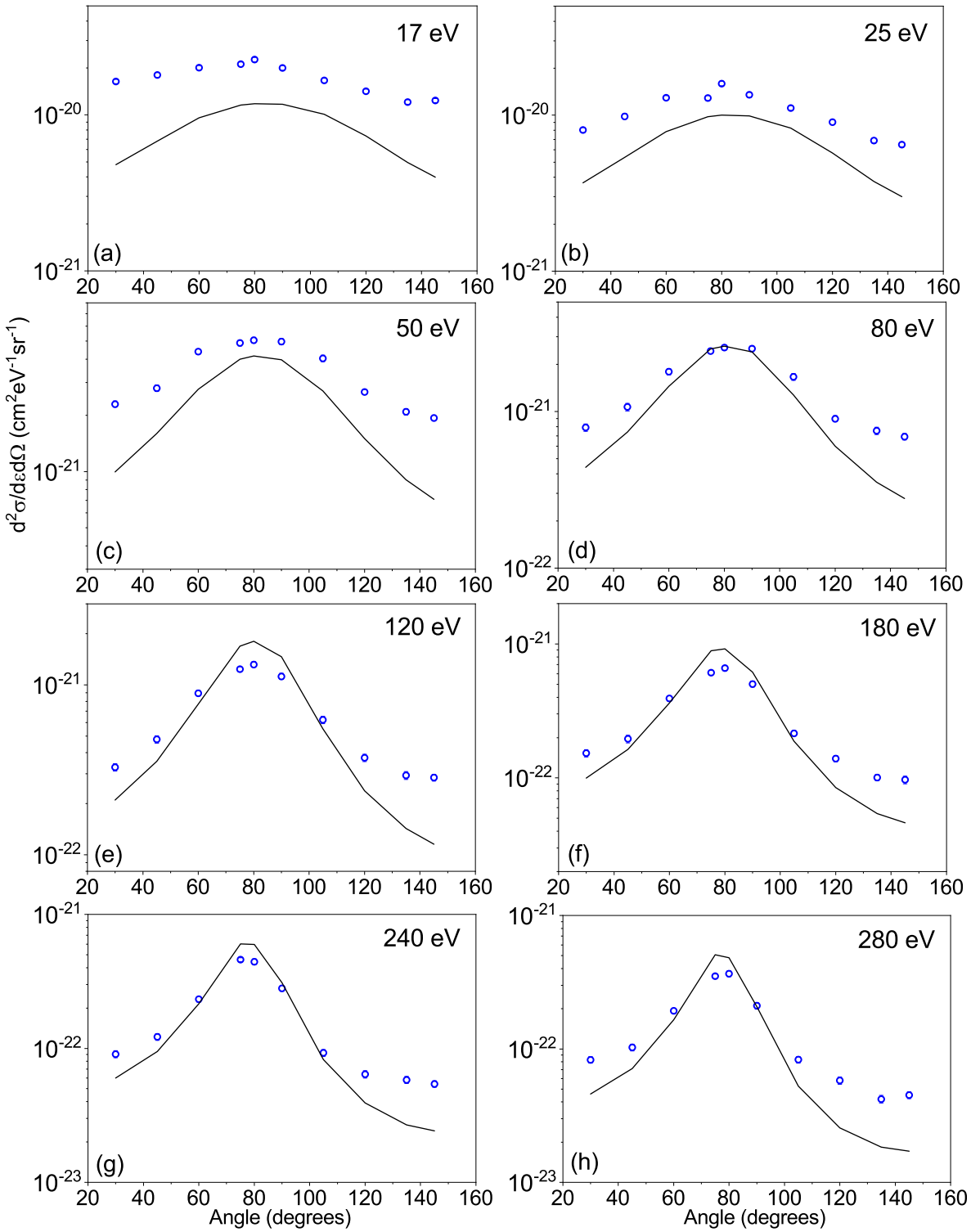


Figure 5.10: Absolute e-DDCS for the collision system 6 keV $e^-$ + $N_2$, at different emission energies. The black solid line represent the CB1 calculations using the RHF/6-311G description of the target wave functions.

model although shows a better agreement with the data, but reveals higher cross sections for the backward angles. In order to understand the deviation in the forward-backward angular asymmetry using the CTMC model and to correct this behavior, some initial tests were per-

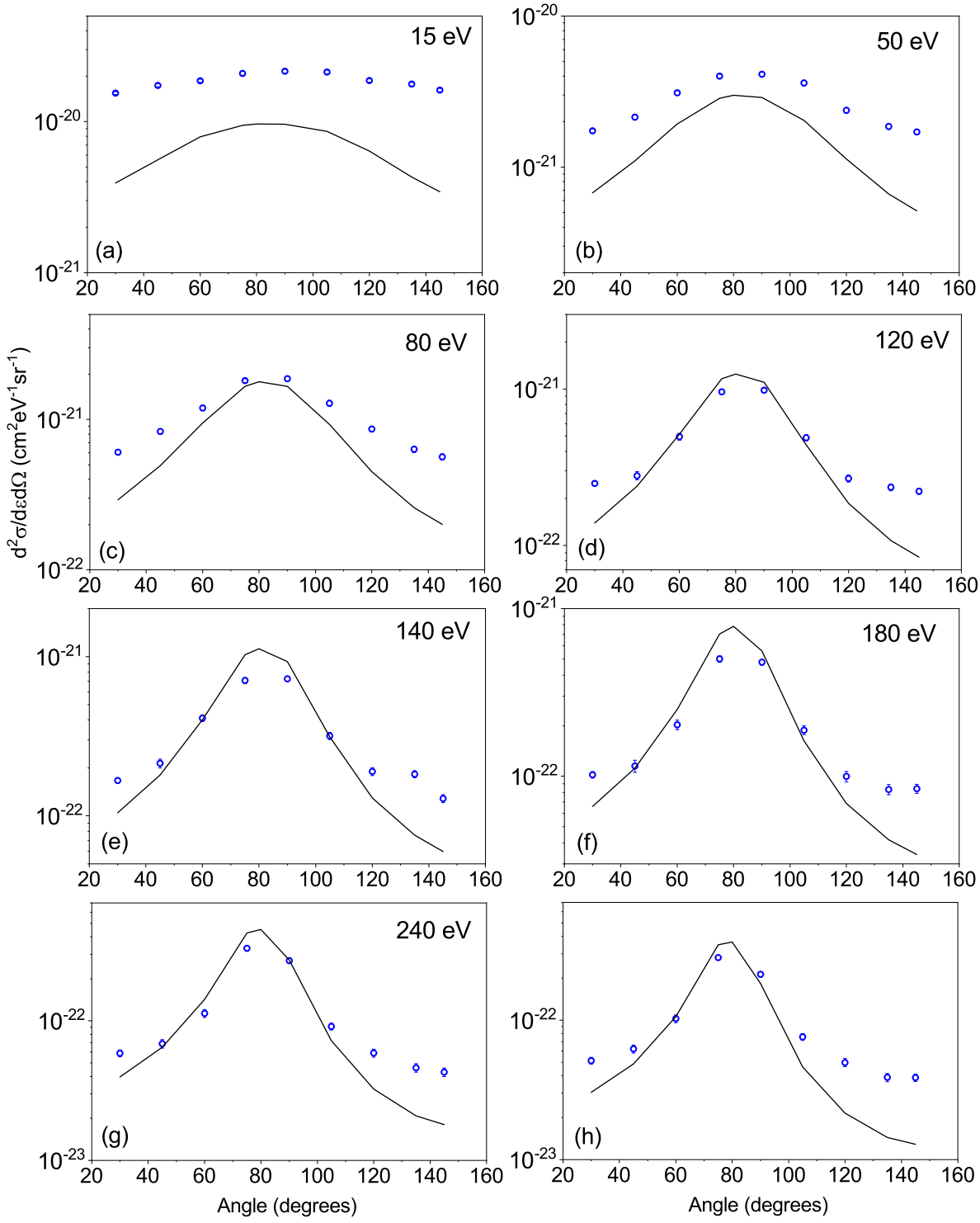


Figure 5.11: Same as Figure 5.10, except for collision system : 8 keV $e^-$ + $N_2$.

formed on the strength of the projectile electron and target electron interactions as modelled in the CTMC approach. As a result of the standard calculations (shown in the figures) the interaction between the two electrons is kept 'ON' during the entire motion of the particles till the asymptotic limit. However, as a initial test the simulations were also performed by switching off the e-e interaction in the exit channel. Although certain improvement were observed in the

distribution, but the results were not conclusive. Thus, the present CTMC model overestimate the strength of the electron-electron interactions particularly in the exit channel. The projectile electron sweep out the ejected target electron from the forward angles to the backward angles.

For all the different beam energies, it is observed experimentally that at higher electron emission energies, forward angles predict slightly higher cross section than its complementary backward angles. For example, in Figure 5.7(f), at ejected electron energy 150 eV, the measured DDCS for forward angle is 1.6 times higher than the backward angle, whereas for 260 eV, the difference goes up to 2.6 times (Figure 5.7(h)). The CB1 model predicts similar kind of angular asymmetry between the forward and backward angles. Such an increase in cross section in the forward angles is generally attributed by the two center effect or due to the non-Coulombic potential for a multielectronic target atom or molecule. In case of electron impact ionization, two center effect does not play a significant role and hence it is mostly due to the non-Coulombic potential of the target molecule that causes the difference in the forward-backward angular asymmetry. In case of ion impact ionization, this difference in forward and backward angles is much larger which will be seen in the next chapter.

## 5.5 Single Differential Cross Section

Integrating the e-DDCS spectrum over the emission energy or emission angle gives us the single differential cross section (SDCS). Integrating over the emission energies, we obtain the SDCS i.e. $d\sigma/d\Omega_e$, as a function of angles which is given by:

$$\frac{d\sigma}{d\Omega_e} = \int \frac{d^2\sigma}{d\Omega_e d\epsilon_e} d\epsilon_e. \tag{5.5}$$

Similarly, integrating over the emission angles, we get the SDCS as a function of the emission energy :

$$\frac{d\sigma}{d\epsilon_e} = \int \frac{d^2\sigma}{d\epsilon_e d\Omega_e} d\Omega_e. \tag{5.6}$$

Figure 5.12 displays the SDCS for all the five beam energies under investigation. The panels on the left column show the SDCS as a function of the emission energies i.e., $d\sigma/d\epsilon_e$, whereas those on the right column represent the SDCS as a function of the ejected angles i.e., $d\sigma/d\Omega_e$. In case of the SDCS varying as a function of emission energies, the CB1 model predicts lower cross sections compared to the data upto $\sim$ 50-60 eV, beyond which one can observe relatively good agreement. This behaviour is seen to be valid for all the five projectile energies. Now, looking into the panels on the right column, it is seen that the CB1 calculations underestimate the measured data for the entire angular spread, with maximum deviations occurring in case of the low forward and high backward angles. The red dashed lines show the CTMC model calculations. The CTMC model is seen to provide an excellent agreement with the measured SDCS

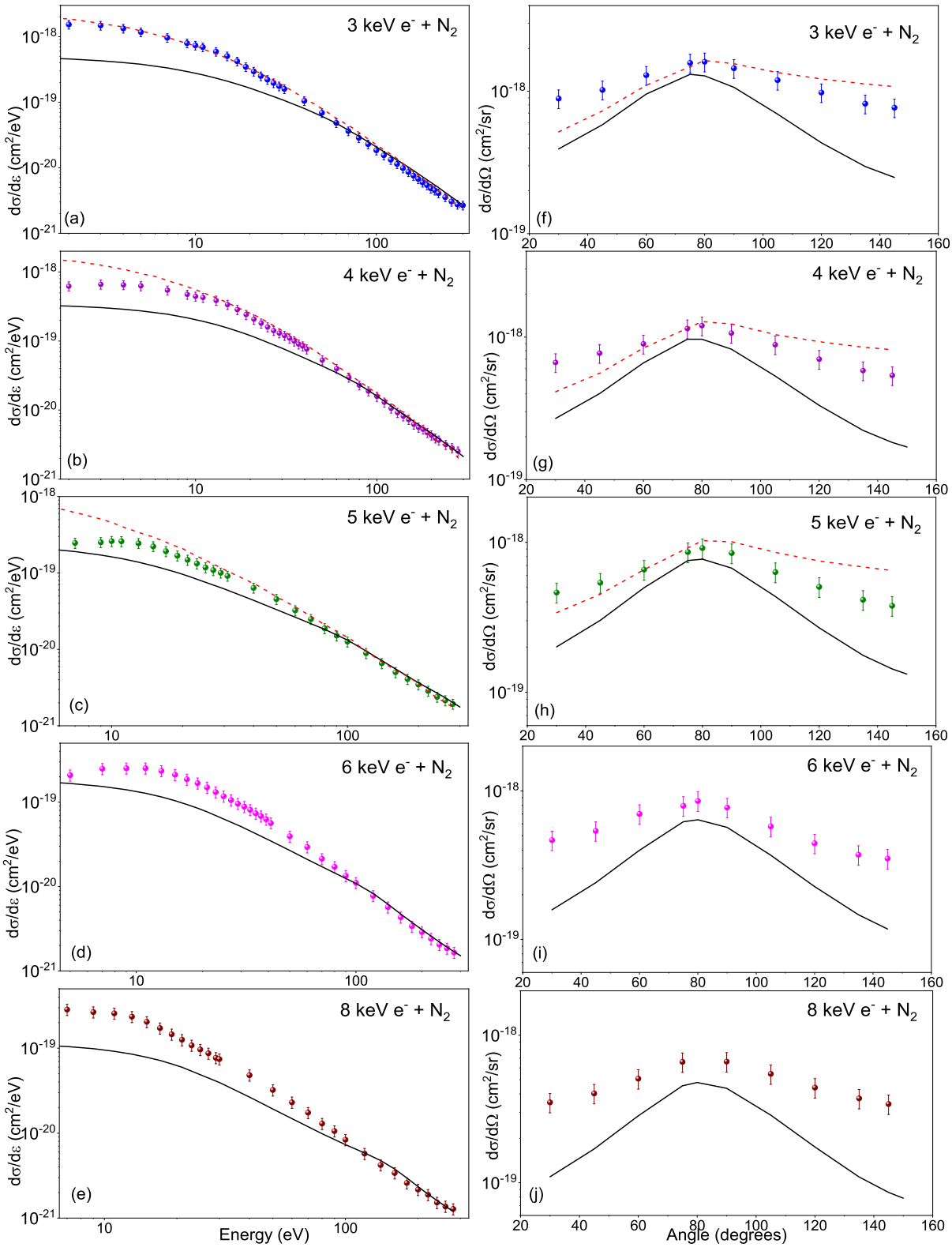


Figure 5.12: The absolute electron SDCS as a function of emission energies (all the panels on the left (a to e)) and function of emission angles (all the panels to the right (f to j)) for different energies of primary electrons colliding with $N_2$. The black solid lines in all the panels represent the CB1 predictions using RHF/6-311G description of the target wave functions. Red dashed lines show the CTMC calculations.

over the entire energy regime (see panels a, b and c). However, minor deviations are observed for the lowest energy electrons in case of 4 and 5 keV (see Figure 5.12(b and c)). Considering the angular distribution plots of SDCS, it is seen that quantitatively the CTMC model shows a much better agreement with the measured data compared to that seen for CB1 model. In case of the forward and intermediate angles (i.e., near the BE peak), the CTMC calculations are in close agreement with the data points, except for the backward angles, where it predicts higher cross sections, showing slightly different characteristics of the forward-backward angular asymmetry. This feature has already been discussed in detail in the previous section.

## 5.6 Total Ionization Cross Section

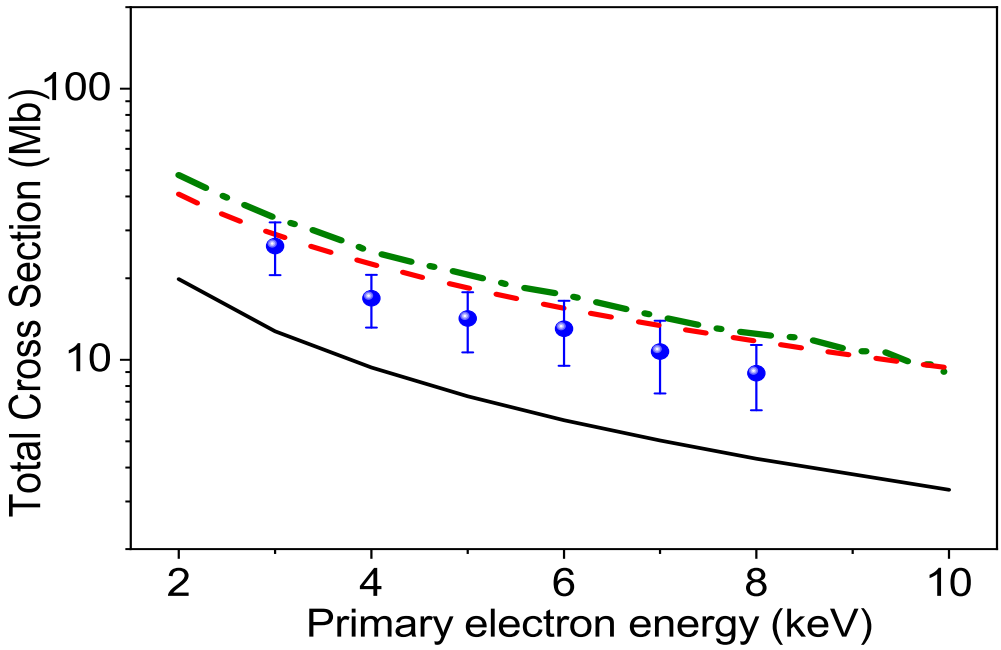


Figure 5.13: Total ionization cross section as a function of incident electron energy along with the predictions of three different models, i.e. the CB1 (black solid line), CTMC (red dashed line) and CSP-ic (green dash-dotted line).

Integrating the SDCS over the emission energies or emission angles gives the total ionization cross section. For the present series of measurements, the TCS were obtained by integrating over the electron energies between 1 and 500 eV and over the emission angles from $\theta$ = $0^0$ to $\theta$ = $180^0$.The data points below $30^0$ and above $145^0$ were estimated by extrapolation to obtain the total cross section. The difference in the TCS after extrapolation was found to be about 11-13%. It was observed that the TCS values derived by integrating the SDCS over the emission angles and energies varied very little i.e. only by $\sim$ 0.3 - 0.4%. In Figure 5.13, the experimental and theoretical TCS values have been displayed which includes the experimentally measured data obtained for 7 keV electron impact on $N_2$[137]. The DDCS measurements for 7

keV electron impact ionization of $N_2$ has already been discussed in the previous chapter.

From Figure 5.13 it is seen that the CB1 model falls well below the present experimentally obtained TCS data but provides an excellent qualitative agreement with the observed energy-dependence. The CTMC model, on the other hand, falls a bit higher compared to most of the data points but mostly within the experimental uncertainties which are about 22-27%. The experimentally obtained TCS values have also been compared with a semi empirical model calculation, namely the complex scattering potential-ionization contribution (CSP-IC) model. This model is used for determining the total ionization cross section of any target molecule when impacted by electrons. In this model, the TCS are calculated based on a complex scattering potential which is constructed with the assumption that the target molecule has a spherical charge density. The complex scattering potential comprises of the real part which takes into account the static, exchange and polarization potentials whereas the imaginary part deals with the absorption term which includes information of the total loss of scattered flux into the allowed channels of electronic excitation and ionization. The form of the different potentials, and further deducing the contribution of the ionization channel from the total inelastic cross sections are explained in details in chapter 3. The TCS values predicted by the CSP-ic model overestimates the measured data for all the energies, but provides a good qualitative behavior regarding the energy dependence (see Figure 5.13). This discrepancy could be due to the consideration of the spherical charge density of the $N_2$ molecule and other approximations [138] used in the semi-empirical model. It is to be noted that the TCS calculations obtained using the two *ab initio* models, (CB1 and CTMC), lie below and just above the experimental values, respectively. The CTMC model provides closest agreement to the present data.

## 5.7 Conclusions

We have measured the absolute DDCS, SDCS and TCS of the secondary electrons emitted from $N_2$ under the impact of 3, 4, 5, 6 and 8 keV fast electrons. The measurements were performed for the emission angles between 30° and 145°. The experimental DDCS spectra have been compared with the CB1 model calculations with two different target wave functions as well as with the CTMC model for twice of atomic nitrogen. No significant difference has been observed between the two sets of the CB1 model calculations corresponding to the two wave functions at the RHF/6-311G and CCSD/cc-pVTZ levels of theory. This suggests that both the wave functions are therefore well equipped to describe the ionization of $N_2$ for the present projectile energy range. The CTMC model provided a very good agreement with the measured data for the entire emission spectra except for certain energy-angle window region. The CB1 model predicted lower cross section values compared to the experimental data for all emission energies, with maximum discrepancy lying in the low emission energy region. Although the CTMC gives the closest representation to the experimental values, the forward-

backward angular asymmetry of the DDCS is not reproduced properly by the CTMC model unlike the CB1 model and hence further investigations are required. The derived TCS values have been compared both with the *ab initio* CB1 and CTMC calculations as well as with the semi-empirical CSP-ic model. While qualitatively both the CB1 and the CSP-ic models show similar energy dependence, the CTMC gives the closest representation to the measured TCS values within experimental uncertainties.